remote sensing

MDPI

Article

Landslide Susceptibility Assessment Based on a Deep Learning-Derived Landslide Inventory in Moxi Town, Sichuan, China

Yitong Yao [1], Yixiang Du [2], Wenjun Zhang [1,3,*], Xianwen Liu [1,3], Jialun Cai [1,3], Hui Feng [1], Hongyao Xiang [4], Rong Hu [1], Yuhao Yang [1] and Tongben Fu [1]

[1] School of Environment and Resources, Southwest University of Science and Technology, Mianyang 621010, China; yaoyitong@mails.swust.edu.cn (Y.Y.); xwliu@swust.edu.cn (X.L.); rscai@swust.edu.cn (J.C.); fhyyds@mails.swust.edu.cn (H.F.); 1402142675@mails.swust.edu.cn (R.H.); yangyuhao@mails.swust.edu.cn (Y.Y.); futb@mails.swust.edu.cn (T.F.)
[2] Sichuan Zhentong Inspection Co., Ltd., Mianyang 621010, China; scztjc@163.com
[3] Mianyang Science and Technology City Division, The National Remote Sensing Center of China, Mianyang 621010, China
[4] School of Civil Engineering and Architecture, Southwest University of Science and Technology, Mianyang 621010, China; xianghongyao@mails.swust.edu.cn
* Correspondence: zhangwenjun@swust.edu.cn

Highlights

What are the main findings?

- Landslide samples were automatically extracted in complex terrain, enabling the construction of landslide inventories for susceptibility assessment and an integrated workflow from automatic landslide identification to susceptibility assessment.
- The deep learning-based and interpretable susceptibility assessment achieved high predictive accuracy in the study area, and identified the dominant controlling factors with their relative contributions.

What are the implications of the main findings?

- Automatically identified landslides can serve as reliable samples for susceptibility modeling in mountainous areas lacking complete historical inventory.
- Susceptibility results combined with factor attribution can support hazard assessment and engineering mitigation planning.

Abstract

Landslides are characterized by strong suddenness and a wide range of damage; accurate prediction of their susceptibility is an important prerequisite for regional risk prevention and control. To address the difficulties in acquiring landslide inventories in complex terrain areas and the insufficient interpretability of existing prediction models, this study proposes a landslide susceptibility assessment (LSA) framework that integrates automated sample detection and interpretability analysis. The proposed framework is applied to Moxi Town, a typical alpine valley area in Sichuan Province, China. A Mask R-CNN instance segmentation model was introduced to achieve automated detection of landslide samples, resulting in a high-quality inventory containing 923 landslides. Based on the spatial relationships between the landslide inventory and influencing factors, a convolutional neural network (CNN) landslide susceptibility assessment model incorporating Shapley Additive exPlanations (SHAP) interpretability analysis was constructed. The CNN model was further compared with random forest (RF) and extreme gradient boosting (XGBoost) machine learning models. The results show that the AUC value of the CNN model has

Check for updates

Academic Editor: Wen Liu

Received: 28 January 2026
Revised: 22 February 2026
Accepted: 6 March 2026
Published: 10 March 2026

Copyright: © 2026 by the authors. Licensee MDPI, Basel, Switzerland. This article is an open access article distributed under the terms and conditions of the Creative Commons Attribution (CC BY) license.

increased by 4.3% and 3.2% compared with the RF and XGBoost models, respectively, and it significantly reduces the pretzel effect of landslide susceptibility mapping (LSM). The results validate the reliability of the proposed framework, which can provide technical support for landslide disaster prevention and monitoring.

Keywords: mask R-CNN; convolutional neural network; SHAP interpretability analysis; landslide detection; landslide susceptibility assessment

1. Introduction

Landslides are one of the major disasters widely distributed in mountainous areas, and their formation mechanisms are controlled by natural factors such as topography, geomorphology, geological structure, and climate change. Human activities further disrupt the original balance of slopes and amplify the risk of instability [1,2]. By the end of 2024, more than 280 thousand potential geological hazards had been identified in China, and landslide areas with medium and high susceptibility accounted for approximately 42% of the total land area. The wide distribution and high incidence of landslide disasters have caused substantial economic losses and posed serious threats to human life and safety [3]. Therefore, it is of great significance to carry out systematic assessment and scientific monitoring of landslide disasters for regional disaster prevention, mitigation, and risk management.

Landslide susceptibility assessment realizes spatial prediction of potential future landslide areas by characterizing the nonlinear relationships between historical landslide distributions and influencing factors, and is one of the most widely used tools for landslide hazard assessment [4,5]. The methodology has gradually evolved from qualitative analysis relying on expert experience to data-driven quantitative modeling, including knowledge-driven, physical, and data-driven methods [6–8]. Knowledge-driven methods are highly subjective and difficult to quantify and objectively evaluate. Physically based models depend on precise geotechnical parameters to analyze slope stability and are difficult to apply at large spatial scales. In contrast, statistical and machine learning models have greater flexibility and applicability within a data-driven framework. Statistical models, such as information values [9], frequency ratios [10], and weights of evidence [11], are difficult to capture the nonlinear coupling between multiple factors, although they have a simple parameterization process and clear physical interpretation. Machine learning models such as random forests [12–14], support vector machines [15,16], and logistic regression [17,18] improve modeling performance to a certain extent; however, the machine learning models still need manual feature construction and have limited ability to exploit complex spatial information structures [19–21].

In recent years, deep learning technology has attracted much attention by virtue of its end-to-end feature learning capability, which makes up for the shortcomings of the insufficient spatial structure of machine learning. Convolutional neural network (CNN), as one of the most representative techniques in deep learning, can learn spatial texture and neighborhood structure directly from the original data, and automatically extract multi-scale abstract features from the shallow to the deep layers to output more accurate prediction results [6]. Relevant studies have shown that CNN models exhibit better prediction ability than traditional models in landslide susceptibility assessment (LSA) [1,22–26]. However, the "black-box" nature of CNN models results in a lack of interpretability. Currently, most relevant studies focus primarily on improving model prediction accuracy. Relying solely on statistical accuracy metrics is insufficient to demonstrate the geological reliability of the

models, and models that consider hierarchical geomorphological relationships of the contributing factors remain lacking. This limitation restricts the applicability of the predictions for targeted disaster management [27–30]. In addition, existing LSA studies mostly rely on manual interpretation or historical records to construct landslide inventories. In areas with complex terrain, such approaches often face difficulties in acquisition and updating delays, which affect sample quality at the source and consequently constrain the reliability of prediction results. In recent years, deep learning semantic segmentation models, such as U-Net and Mask R-CNN, have been applied to automatic landslide extraction, improving landslide identification efficiency and accuracy [29,30]. However, most of these studies focus on landslide detection itself and do not further explore how the detection results serve landslide susceptibility assessment or influence prediction performance [31–33].

Based on a comprehensive consideration of both the quality of the landslide inventory and the interpretability of the model, in this study, a unified framework was developed for Moxi Town, integrating automatic landslide detection, susceptibility modeling, and interpretable analysis using SHAP. The Mask R-CNN instance segmentation model was employed to accurately identify landslide samples, improving the quality and reliability of the inventory for susceptibility assessment. Based on this, a CNN model with SHAP interpretability analysis was developed for landslide susceptibility evaluation, using the inventory and 14 influencing factors related to topography, hydrometeorology, and human activities as input. The results provide scientific references for landslide susceptibility research and regional disaster prevention.

2. Study Area and Data

2.1. Study Area

Moxi Town is located in the central part of Luding County, Ganzi Tibetan Autonomous Prefecture, Sichuan Province (longitude 101.87° to 102.17°E, latitude 29.52° to 29.69°N), as shown in Figure 1. It is situated in the northeastern part of the Moxi Fault, which forms the southern part of the highly active Xianshuihe Fault Zone. Long-term faulting activity has formed a complex geological foundation, providing abundant material sources for landslide occurrence. The topography of the region exhibits typical high-mountain valley geomorphology, with towering mountains and steep slopes, deeply incised river valleys, intense river downcutting and steep slopes (maximum gradient up to 80°), forming a large relative elevation difference, as shown in Figure 1c, reducing slope stability. The steep geographic features and complex geological structure make Moxi Town a highly developed area for landslide hazards.

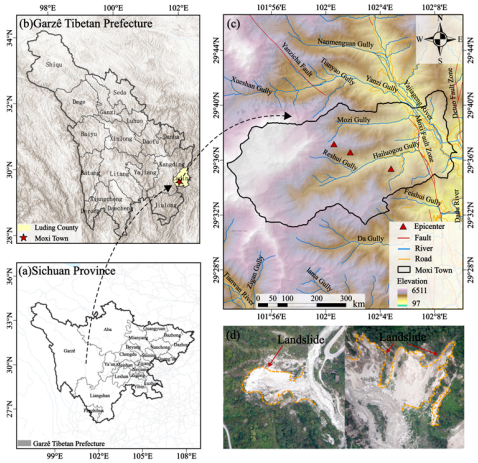


Figure 1. Study area: (**a**,**b**) geographical location of the study area; (**c**) topography and tectonic background; (**d**) example of current landslide distribution.

2.2. Data Sources

2.2.1. Landslide Dataset

The landslide dataset formed the foundation for analyzing the spatial distribution characteristics of landslides and for developing reliable susceptibility models. In this study, a hybrid strategy was used to construct a landslide dataset, which consisted of a public dataset and a study-area-oriented self-compiled dataset. The public dataset was selected from a multi-sensor dataset previously used for landslide detection modeling [31]. To ensure regional applicability, the public dataset was used after uniform correction of spatial boundaries and location information. Meanwhile, based on the high-precision visual interpretation of Jilin-1 remote sensing images of Moxi Town acquired from November to December 2022, landslide boundaries were manually delineated using polygon annotation in Labelme5.7.0, and a self-compiled landslide dataset with instance segmentation labels was constructed to supplement and refine the landslide information in the study area. All annotated results were converted into COCO format to meet the training requirements of the Mask R-CNN model. Finally, a landslide dataset consisting of 7472 image patches of 512 × 512 pixels was constructed. Detailed information on the dataset is provided in Table 1. The dataset was randomly divided into training, validation, and test sets at a ratio of 7:1.5:1.5 for model training and performance evaluation.

Table 1. Detailed information on the landslide dataset.

Dataset Type	Acquisition Platform	Sample Area	Sample Quantity (Images)	Spatial Resolution (m)
Public Dataset	UAV	Moxi Town	1795	0.2/1
	Landsat	Wenchuan	178	5
	Sentinel-2/L2A	Moxitaidi	652	0.6
	SuperView-1	Mengdong Town	1155	0.5
	GF-1	Longxi River	1769	0.5
Self-Compiled Dataset	Jilin-1	Moxi Town	1923	0.5

2.2.2. Landslide Conditioning Factors

The occurrence of landslides is often influenced by a variety of triggering conditions, including topography, geology, and other factors. Landslide susceptibility assessment is conducted based on historical landslide events, under the assumption that future landslides are likely to occur under environmental conditions similar to those observed in the past, so selecting appropriate influencing factors as model inputs is crucial for landslide susceptibility analysis. In this study, fifteen landslide conditioning factors (LCFs) were selected based on conditioning factors widely adopted in previous landslide susceptibility studies, in combination with the regional characteristics of Moxi Township, including active tectonic settings, pronounced topographic relief, and abundant rainfall, as shown in Table 2.

The above 15 factor layers were uniformly aligned to the UTM Zone 48N projection under the WGS1984 coordinate system, and their data formats were unified as raster data with a spatial resolution resampled to 30 m. The factor thematic maps are shown in Figure 2. To eliminate differences in magnitude and value ranges among the evaluation factors and to ensure that all factors had comparable weights and contributions during the model training process, all factors were uniformly normalized and scaled to the range of 0–255.

Table 2. Detailed information on LCFs.

Factors	Format	Source	Spatial Resolution
Altitude, slope, aspect, plane curve, profile curve, TWI, TRI	Raster	ALOS-PALSAR-DEM (https://search.asf.alaska.edu/, accessed on 1 December 2025)	12.5 m
Dis_road, Dis_river	Vector	1:50,000 National Fundamental Geographic Information (https://www.webmap.cn/main.do?method=index, accessed on 1 December 2025)	1:5 W
LULC	Raster	GlobeLand30 Dataset (https://www.webmap.cn/main.do?method=index, accessed on 1 December 2025)	30 m
NDVI	Raster	2000–2022 China 30 m Annual Maximum NDVI Dataset (https://www.escience.org.cn/, accessed on 1 December 2025)	30 m
Rainfall	NETCDF	China 1 km Resolution Monthly Precipitation Dataset (https://data.tpdc.ac.cn/home, accessed on 1 December 2025)	1 km
Lithology, Dis_fault	Vector	1:200,000 National Geological Spatial Database (https://www.tianditu.gov.cn/, accessed on 1 December 2025)	1:20 W
PGA	.xls	Mainland China M4.0+ Earthquake Strong Motion Parameter Dataset (https://data.earthquake.cn/index.html, accessed on 1 December 2025)	/

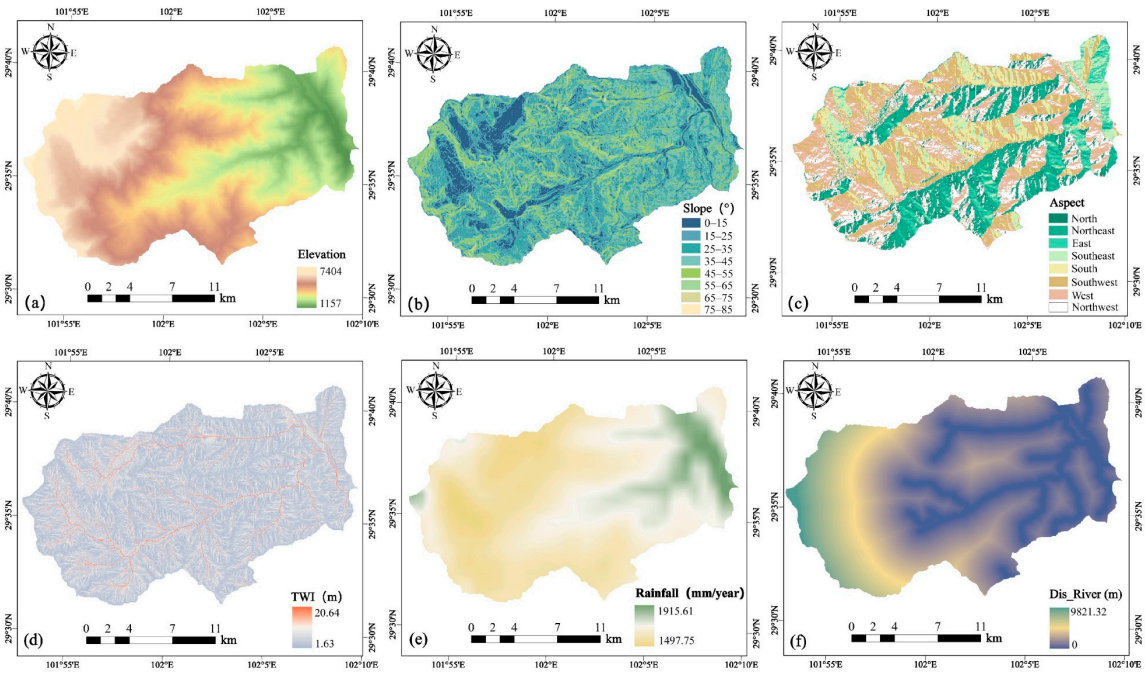


Figure 2. *Cont.*

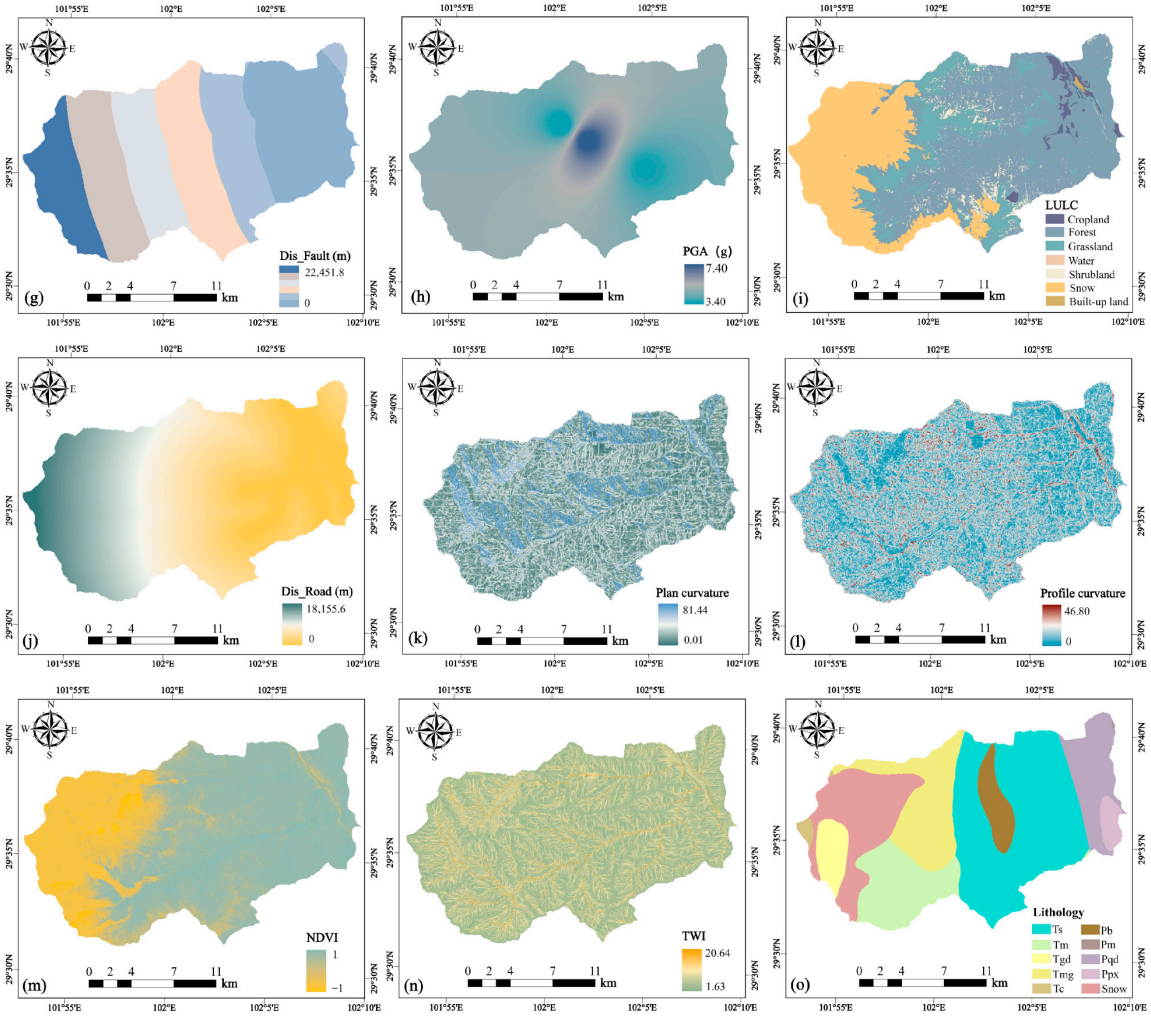


Figure 2. Thematic maps of factors: (**a**) altitude; (**b**) slope; (**c**) aspect; (**d**) TRI; (**e**) rainfall; (**f**) dis_river; (**g**) dis_fault; (**h**) PGA; (**i**) LULC; (**j**) dis_road; (**k**) plane curve; (**l**) profile curve; (**m**) NDVI; (**n**) TWI; (**o**) lithology.

3. Methodology

This study aims to develop an interpretable framework for landslide susceptibility assessment by integrating deep learning-based landslide detection. The overall workflow of the proposed framework is illustrated in Figure 3 and consists of three main stages.

First, a Mask R-CNN model is constructed for automatic landslide detection. The optimal detection performance is achieved by evaluating different combinations of backbone networks and optimizers, resulting in high-quality landslide samples with precise boundaries. Meanwhile, effective landslide conditioning factors (LCFs) are selected based on multicollinearity diagnostics and importance analysis. Subsequently, CNN, RF, and XGBoost models are developed to capture the spatial relationships between landslide samples and influencing factors, and corresponding landslide susceptibility maps (LSMs) are generated. Finally, the prediction results are evaluated using both qualitative and quantitative approaches.

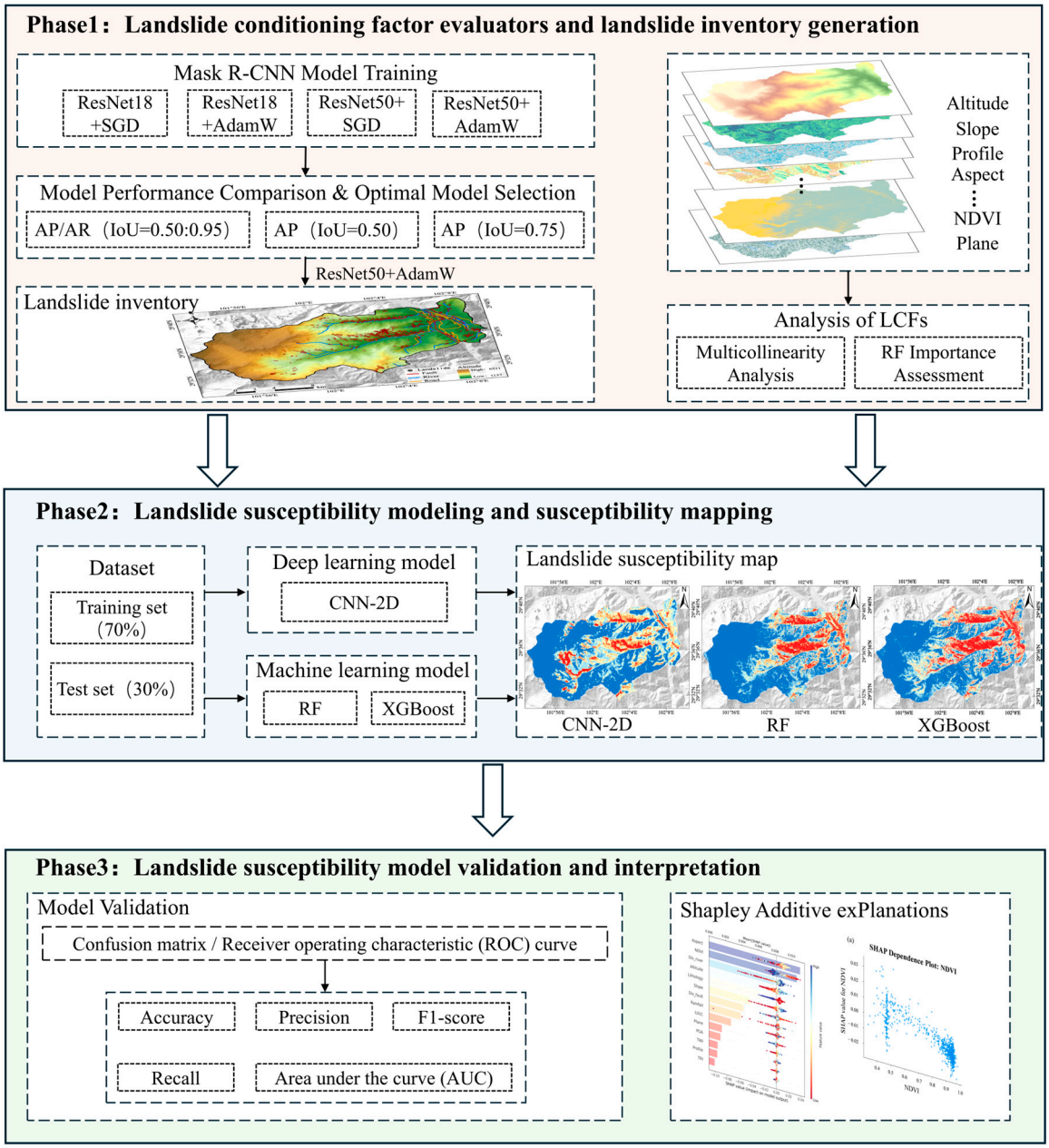


Figure 3. Flowchart of the framework in this study.

3.1. Landslide Detection

3.1.1. Mask-RCNN

Mask R-CNN is a two-stage instance segmentation model that extends Faster R-CNN by introducing a fully convolutional network (FCN) branch for mask prediction. It consists of four core modules: backbone network, region proposal network (RPN), region of interest align (RoI Align), and head network [32–34], as shown in Figure 4. In the first stage, the model uses a backbone network composed of a residual network (ResNet) and a feature pyramid network (FPN) to extract multi-scale features. The RPN scans the feature maps using predefined anchor boxes and performs foreground–background classification and bounding box regression for each anchor. Candidate regions of interest (RoIs) are then generated through non-maximum suppression (NMS) [35]. In the second stage, to avoid information loss caused by coordinate quantization in the traditional region of interest pooling (RoI Pooling) layer, the RoI Align layer is adopted to achieve precise alignment between RoI features and the corresponding feature maps [36–38]. Subsequently, the head

network processes the RoI features in parallel. Its Box Head branch generates the object class probability and bounding box coordinate prediction for each RoI, while the FCN branch generates a pixel-level segmentation mask for each RoI [39].

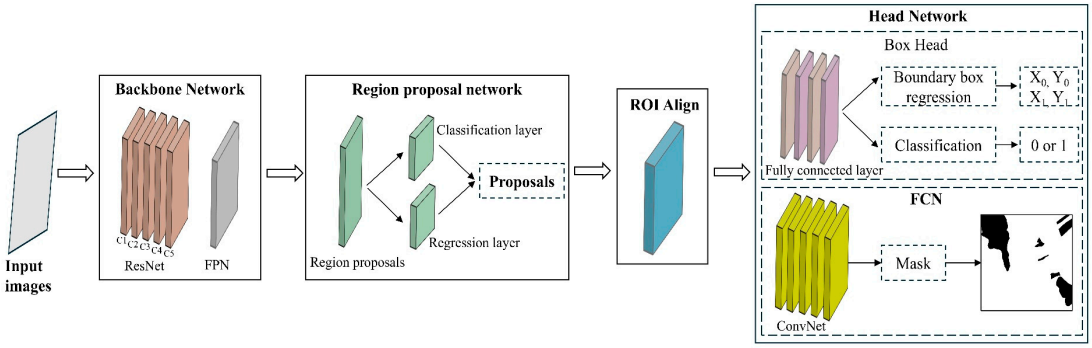


Figure 4. The architecture of the Mask R-CNN landslide detection model.

To alleviate the large variability in landslide morphology within the study area, a composite data augmentation strategy was adopted during model training. Specifically, random flipping, random erasing, scaling, and color perturbation were applied to increase sample diversity and enhance feature representation, thereby improving the model's generalization ability and robustness under complex terrain conditions. In addition, Mask R-CNN models with different combinations of backbone networks (ResNet18/ResNet50) and optimizers (SGD/AdamW) were constructed to assess the influence of model configurations on recognition performance. The detailed hyperparameter configurations are listed in Table 3.

Table 3. Hyperparameter settings for Mask R-CNN model training.

Learning Rate Scheduler	Initial Learning Rate	Minimum Learning Rate	Weight Decay	Bacth_Size	Epoch
Cosine Annealing	1×10^{-3}	5×10^{-6}	0.5	8	100

3.1.2. Performance Evaluation of the Landslide Detection Model

In this study, the COCO evaluation system is used to quantitatively assess the performance of the landslide detection model. The evaluation metrics include the average precision for bounding box detection (AP_b) and the average precision for instance segmentation (AP_s), as well as their variants AP_{b50}, AP_{b75}, AP_{s50}, and AP_{s75} under different IoU thresholds. The AP is obtained by calculating the integral area of the precision–recall curve over multiple IoU thresholds (IoU = 0.50:0.95), and a value closer to 1 indicates better overall model performance. AP_{b50}/AP_{s50} and AP_{b75}/AP_{s75} represent the detection and segmentation performance at IoU thresholds of 0.50 and 0.75, respectively. The average recall metrics, for instance, segmentation (AR_s) and detection (AR_b), are used to reflect the completeness of landslide sample recognition by the model [40]. The COCO evaluation framework enables a comprehensive assessment of the Mask R-CNN model with respect to detection accuracy and completeness, thereby ensuring the reliability and robustness of the constructed landslide inventory.

3.2. Evaluation of Conditioning Factors

3.2.1. Multicollinearity Analysis

Landslide susceptibility assessment is based on the assumption that the variables are independent of each other. If strong linear correlations exist among the selected

factors, it is easy to lead to the redundancy of the factor information, thus potentially distorting the results of the assessment. Therefore, it is necessary to test for multicollinearity among the factors before model construction [41–43]. In this study, tolerance (TOL) and variance inflation factor (VIF) analyze the correlation among factors. Assuming that $X = \{X_1, X_2, \ldots, X_n\}$ represents a set of independent variables, R_j^2 represents the coefficient of determination of the j variable X_j when it is regressed on all other predictor variables in the model. The VIF is calculated as follows:

$$VIF = \frac{1}{1-R_j^2} \quad (1)$$

The TOL value is the reciprocal of the VIF and reflects the degree of linear correlation among independent variables. In general, VIF values are greater than 1, and TOL values range between 0 and 1. When $VIF > 10$ or $TOL < 0.1$, strong multicollinearity among the factors is indicated [44,45].

3.2.2. Importance Analysis

In this study, the random forest (RF) algorithm is employed to evaluate the importance of landslide influencing factors, and the factors with strong predictive capability are selected as input features for model construction, thereby improving both the prediction accuracy and interpretability of the model [46]. Random forests achieve robustness analysis by integrating multiple decision trees, and their assessment of factor importance is mainly based on two approaches. The first is Gini impurity importance, which is used to measure the contribution of each factor to the node splitting of a decision tree, where a larger reduction in Gini impurity indicates higher importance. The second is the importance of permuting, which is reflected by the improvement in prediction error after randomly permuting the factor values.

3.3. Landslide Susceptibility Assessment

3.3.1. CNN

In landslide susceptibility assessment, the occurrence probability of landslides in each grid unit is related to multiple influencing factors, and each grid unit is characterized by a set of attribute features representing its potential susceptibility. To incorporate one-dimensional influencing factors into the CNN framework, this study constructed a 9×9 neighborhood window centered on each grid unit and stacked all the influencing factors in the region to finally form an input tensor with a size of $9 \times 9 \times 14$. In this way, the landslide susceptibility modeling problem was transformed into a spatial feature learning task suitable for CNN-based analysis.

CNN extracts and combines local features by layering to portray complex spatial patterns [47,48]. The CNN model constructed in this study consisted of two convolutional modules and one fully connected layer, as shown in Figure 5. The first convolutional layer used 32 convolutional kernels of size 3×3 to process the input features. After ReLU activation and batch normalization, the feature maps were downsampled to 4×4 through a 2×2 max-pooling layer. The second convolutional layer contained 64 convolutional kernels of size 3×3 to further extract deeper features, producing feature representations of $2 \times 2 \times 64$ after the second pooling operation. To improve the generalization ability of the model, dropout regularization with a dropout probability of 0.2 was introduced after both layers of the convolution modules. Finally, the feature maps were flattened and input into the fully connected hidden layer containing 128 neurons, and after dropout regularization with a dropout probability of 0.3, the output layer completed the mapping of features to task output.

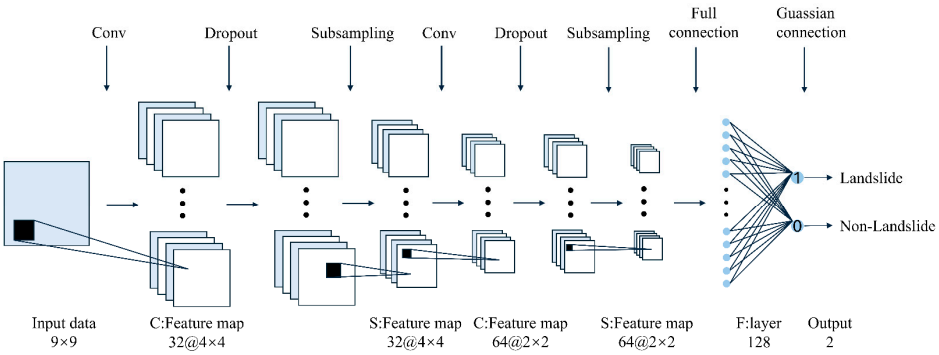


Figure 5. The architecture of the CNN-based landslide susceptibility model.

3.3.2. Performance Evaluation of Landslide Susceptibility Models

For constructed landslide susceptibility models, a comprehensive evaluation based on test data is essential. Landslide susceptibility assessment is a classical binary classification problem. In this study, six quantitative metrics were derived from the confusion matrix to evaluate the model performance, namely, accuracy, precision, F1-score, recall, receiver operating characteristic (ROC) curve, and area under the curve (AUC); values of these metrics closer to 1 indicate better model performance [49–51]. Among them, the ROC curve is a kind of comprehensive indicator to measure the model specificity and sensitivity, whose horizontal axis represents 1—specificity, and the vertical axis represents sensitivity, indicating the model's ability to distinguish between landslide and non-landslide samples, respectively [52]. The performance metrics are calculated as follows:

$$Accuracy = \frac{TP+TN}{TP+TN+FP+FN} \quad (2)$$

$$Precision = \frac{TP}{TP+FP} \quad (3)$$

$$F1-score = \frac{2TP}{2TP+FP+FN} \quad (4)$$

$$Recall = \frac{TP}{FN+TP} \quad (5)$$

$$Specificity = \frac{TN}{TN+FP} \quad (6)$$

$$Sensitivity = \frac{TP}{TP+FN} \quad (7)$$

where TP and TN represent the number of correctly classified landslide and non-landslide samples, while FP and FN denote the numbers of non-landslide and landslide samples that are incorrectly classified.

3.4. Shapley Additive exPlanations

Most advanced algorithms are "black box" models that lack interpretability. SHAP is an interpretability analysis method that can be used to reveal the prediction results of "black box" models, thereby improving the credibility and transparency of the models [53,54]. The core of the SHAP algorithm is to compute the contribution of each feature to the model output using the Shapley value in game theory, which accurately measures how the features drive the prediction. For a feature x_i in the feature set S, the Shapley value is calculated as follows:

$$\varnothing_i = \sum_{S \subseteq F \setminus \{i\}} \frac{|S|!(|F|-|S|-1)!}{|F|!} [f_x(S \cup \{i\}) - f_x(S)] \quad (8)$$

where F represents the set of all features; S represents any subset of features that does not contain feature i; $|S|$ represents the number of features in set S; $f_x(S)$ represents the contribution to the predicted output of the model when only the feature set S is used;

and $f_x(S \cup \{i\})$ represents the contribution to the predicted output of the model from the feature set that contains feature i.

4. Results

4.1. Mask R-CNN-Based Landslide Detection

In this study, Mask R-CNN models with different combinations of backbone networks (ResNet18/ResNet50) and optimizers (SGD/AdamW) were constructed and evaluated using the same landslide dataset. The final test results are shown in Table 4. Based on COCO metrics, under the same optimizer settings, the deeper ResNet50 backbone exhibited stronger feature representation ability than ResNet18. When the optimizer was AdamW, the AP_s and AP_b of ResNet50 compared to ResNet18 increased by 3.8% and 5.5%, respectively. When the optimizer was SGD, the performance of ResNet50 was even more significant, with AP_s and AP_b increasing by 3.5% and 7.1%, respectively. In terms of optimizer comparison, the adaptive tuning strategy of AdamW as the model optimizer can avoid the model from falling into local optimal solutions. When the backbone network was ResNet18, the AdamW optimizer increased AP_s and AP_b by 8.4% and 7.7%, respectively, compared with SGD; when the backbone network used ResNet50, AP_s and AP_b increased by 8.7% and 6.1%, respectively. In terms of recall (ARs/ARb), the ResNet50 + AdamW combination achieved the highest values, reaching 70.6% and 80.7%, respectively, indicating superior coverage of landslide targets. Regarding conventional accuracy metrics (precision/F1-score), the same combination attained a precision of 90.3% and an F1-score of 84.7%, further confirming its reliability and overall performance advantage in landslide detection.

Table 4. Comparison of the accuracy of different backbone networks and optimizers on the test set.

Backbone + Optimizer	AP_s (%)	AP_{s50} (%)	AP_{s75} (%)	AP_b (%)	AP_{b50} (%)	AP_{b75} (%)	AR_s (%)	AR_b (%)	Precision (%)	F1-Score (%)
ResNet18 + SGD	38.4	73.4	37.7	50.4	77.4	56.4	60.2	72.6	68.0	69.3
ResNet18 + AdamW	46.8	78.1	52.5	58.1	81.0	66.1	63.3	75.2	72.5	73.4
ResNet50 + SGD	41.9	77.1	43.6	57.5	81.1	65.8	60.5	75.6	73.9	73.8
ResNet50 + AdamW	50.6	81.1	58.1	63.6	83.8	73.2	70.6	80.7	90.3	84.7

Figure 6 shows representative images from the test dataset and their prediction results. Compared with ResNet18 (columns b and c), the ResNet50 backbone (columns d and e) detected more complete landslide extents, and the generated segmentation masks exhibited higher spatial consistency with the actual landslide boundaries. In addition, the AdamW optimizer (columns c, e) performed better in terms of the recall and confidence of landslide targets compared to SGD (columns b, d). Overall, the combination of ResNet50 and AdamW achieved the best performance in the landslide detection task. It not only detected more landslide boundaries but also effectively distinguished between landslides and interfering features, and the segmentation mask accurately fitted the actual boundaries of the landslide without cross-confusion.

After the landslides were initially detected using the optimal model, a total of 923 landslides were retained to construct the landslide inventory of the study area by overlaying with the corresponding layers for verification. The detected landslides were mainly shown characterized by thin, light-yellow strip-like features on the remote sensing images, mostly located on both sides of the Moxi Fault zone or in the places where there are intensive human activities. The spatial distribution of the landslides in the study area is shown in Figure 7.

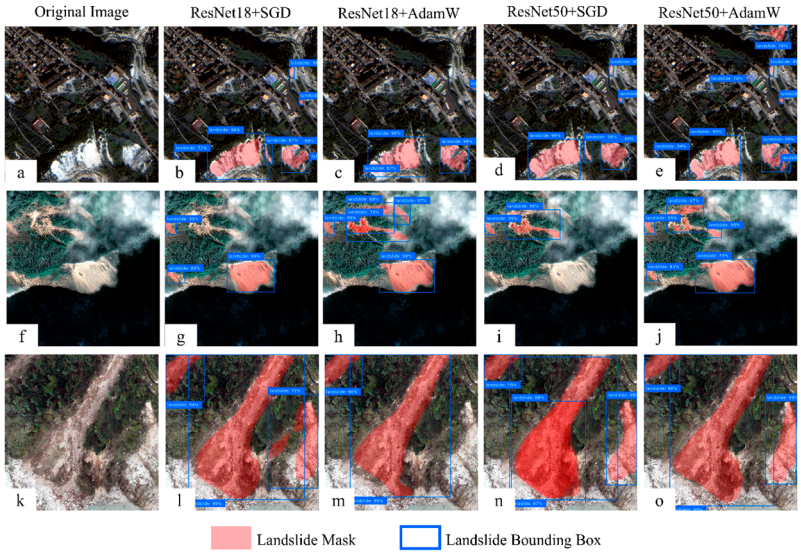


Figure 6. Landslide detection results for different backbone networks and optimizers on the test dataset: (**a**,**f**,**k**) original image; (**b**,**g**,**l**) ResNet18+SGD; (**c**,**h**,**m**) ResNet18+AdamW; (**d**,**i**,**n**) ResNet50+SGD; (**e**,**j**,**o**) ResNet50+AdamW.

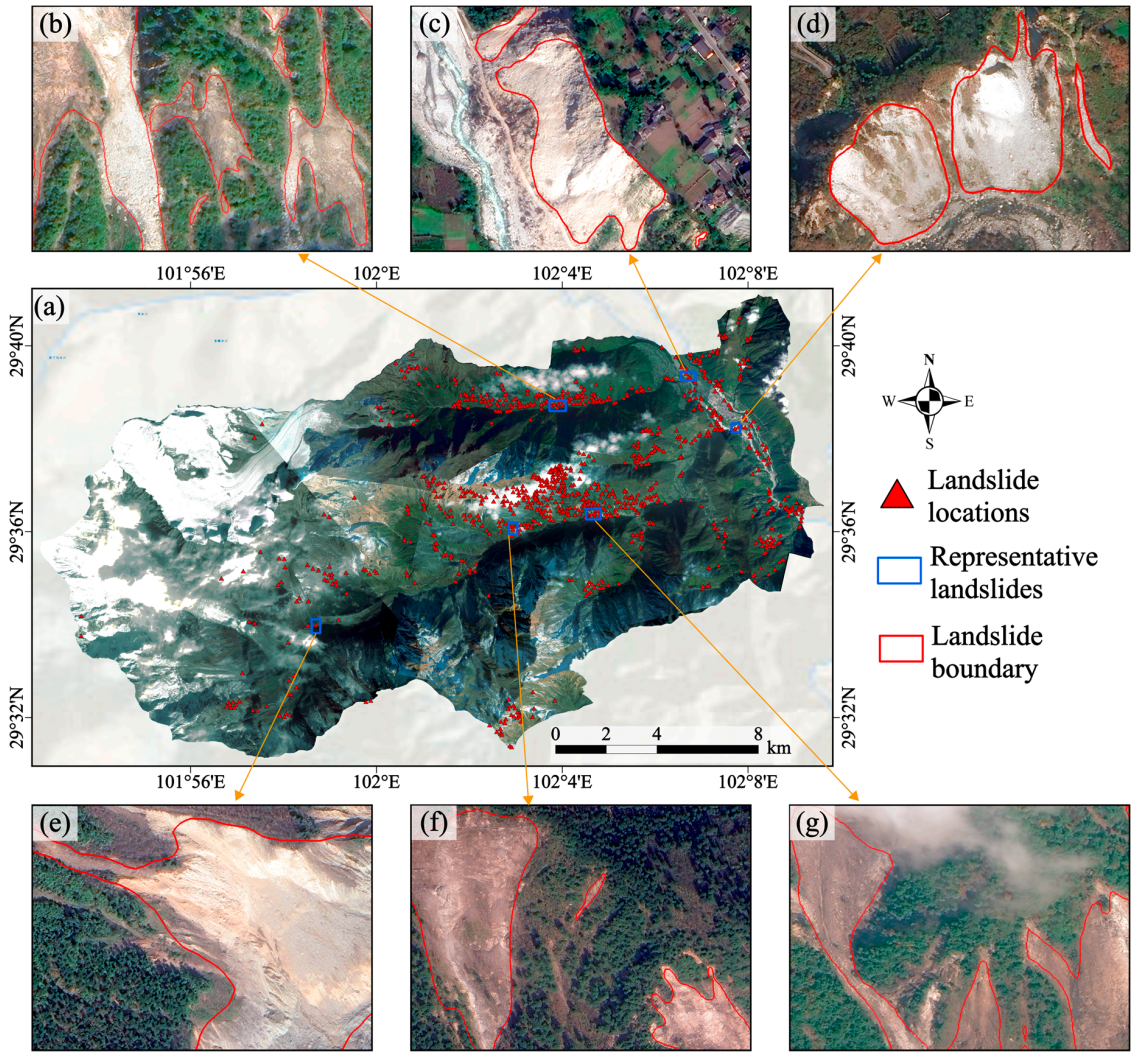


Figure 7. Inventory of landslides in Moxi Town: (**a**) shows the distribution of landslides; (**b**–**g**) shows the typical landslides on remote sensing images.

Compared with the 704 landslides recorded in the town of Moxi, a total of 923 landslides were detected in this study using Mask R-CNN followed by correction, covering a broader range of landslide occurrences. Considering the model performance metrics, the deep learning-based landslide inventory demonstrated high quality, which partially compensated for the incompleteness of manual inventories in the alpine canyon area and provided an effective supplement and extension to the existing landslide records.

4.2. LCFs Selection

The results of the factor multicollinearity and importance analysis are shown in Figure 8. The VIF values of all factors ranged from 1.05 to 15.47, and the TOL values ranged from 0.06 to 0.96, among which the VIF values of distance to fault (VIF = 14.95; TOL = 0.07), distance to road (VIF = 15.47; TOL = 0.07), and altitude (VIF = 11.83; TOL = 0.09) exceeded 10; the TOL values were lower than 0.1, indicating a high degree of multicollinearity among these three variables. According to the importance ranking of the factors, among the three factors with a VIF greater than 10, distance to road had the lowest importance. Therefore, to retain variables with higher predictive contributions while controlling multicollinearity, distance to road was excluded from the final model. After its removal, multicollinearity was reassessed for the remaining factors, and all VIF values were below the critical threshold of 10, indicating that the multicollinearity issue had been effectively addressed.

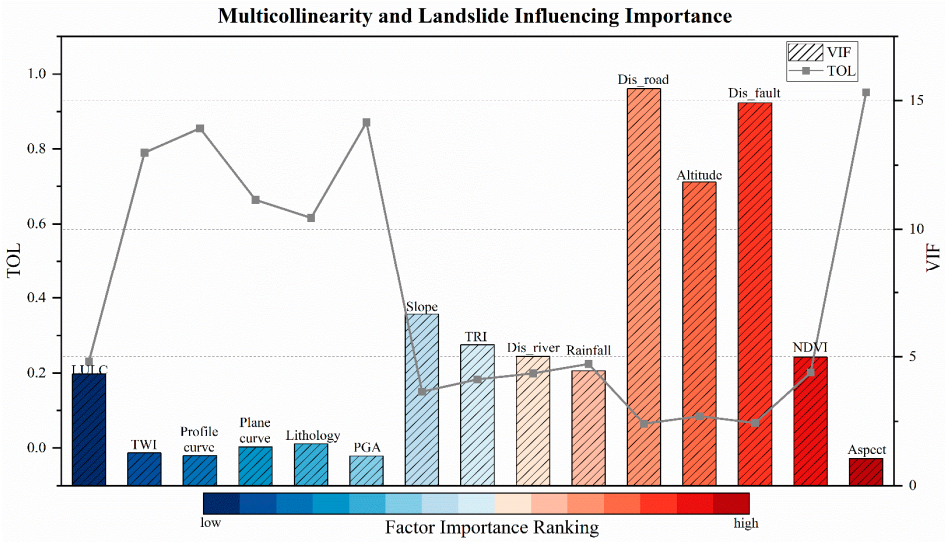


Figure 8. Multicollinearity and significance analysis for LCFs.

4.3. Landslide Susceptibility Map

In this study, the probability of landslide occurrence was predicted for each raster unit in the study area based on the CNN model, and the RF and XGBoost machine learning models were introduced for comparative analysis to verify the reliability of the proposed approach. The Landslide Susceptibility Index (LSI) of each raster unit was calculated using the three trained models, where higher LSI values indicated a higher probability of landslide occurrence. In order to better explain the landslide susceptibility of the study area, the natural breaks were used to classify the LSI into five grades: low, very low, medium, high, and very high. The LSI of each raster unit was spatially visualized in the ArcGIS 10.4.1 environment to generate landslide susceptibility maps. The results of the susceptibility mapping for different models are shown in Figure 9.

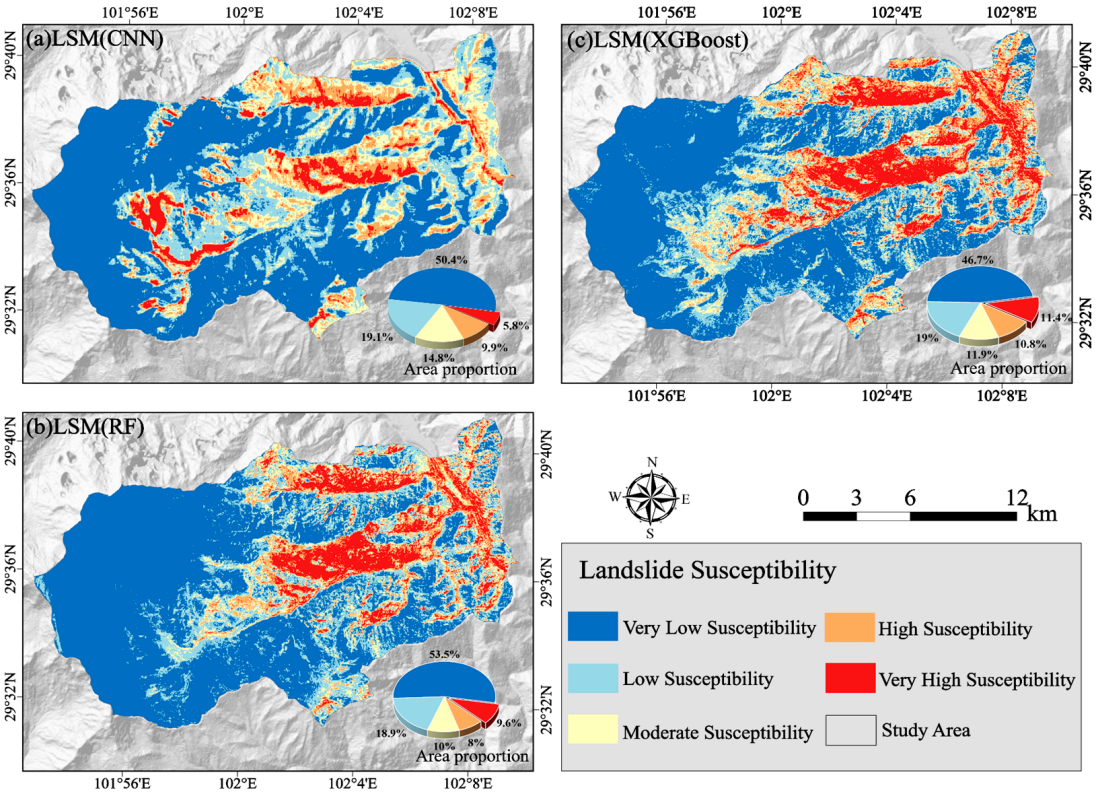
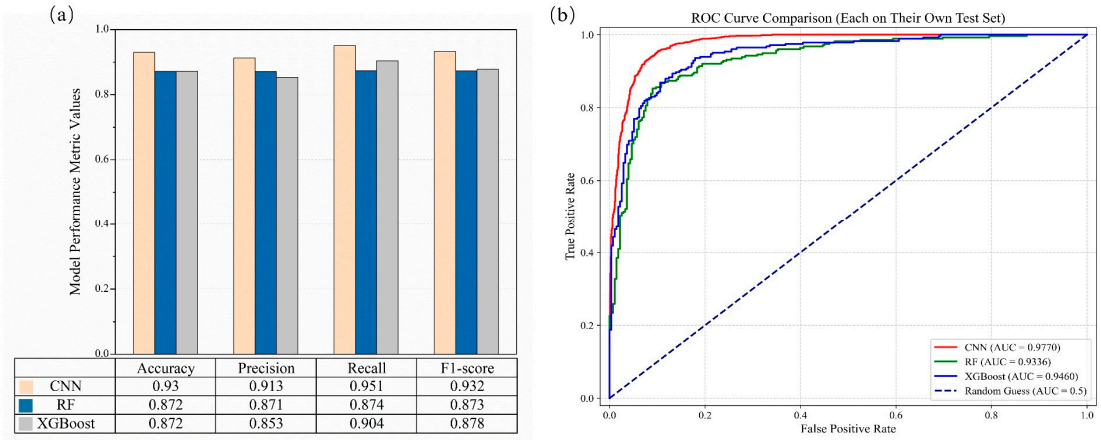


Figure 9. LSM of Moxi Town: (**a**) CNN model; (**b**) RF model; (**c**) XGBoost model.

According to Figure 9, the spatial distribution patterns of landslide susceptibility derived from the three models are generally similar. Very low and low susceptibility zones were mainly distributed in the western part of the study area, whereas high and very high susceptibility zones were concentrated in the central and eastern regions. However, clear differences were observed in the area proportion and spatial continuity of susceptibility classes among the models. The proportions of high and very high susceptibility zones predicted by the CNN, RF, and XGBoost models were 15.67%, 17.56%, and 22.27%, respectively. In terms of spatial expression, the LSM boundaries of the CNN model were naturally smooth, with very high and high susceptibility zones distributed in bands or slices, and relatively smooth transitions between susceptibility classes. This was more consistent with the characteristics of regional landslide continuity. In contrast, the RF and XGBoost results showed fragmented patches, frequent class changes between adjacent pixels, and salt-and-pepper noise in local areas.

4.4. Landslide Susceptibility Model Validation and Comparison

In this study, the performances of the three models were evaluated using the test set. As shown in Figure 10a, the CNN model achieved the best performance. Its accuracy increased to 0.93, and the rest of the metrics were better than the XGBoost and RF models. To avoid the limitations of a single evaluation metric, the overall performance of the three models was further evaluated using ROC–AUC. Figure 10b shows the ROC-AUC of each model, with all AUC values exceeding 0.90, among which the CNN model achieved the highest AUC value of 0.97, representing an increase of approximately 4.65% over the random forest model and 3.28% over the XGBoost model. In terms of prediction accuracy and overall performance, the CNN model exhibited better prediction ability.



	Accuracy	Precision	Recall	F1-score
CNN	0.93	0.913	0.951	0.932
RF	0.872	0.871	0.874	0.873
XGBoost	0.872	0.853	0.904	0.878

Figure 10. Model test results: (**a**) comparison of metrics; (**b**) ROC.

Furthermore, spatial partition validation was conducted to reduce the spatial autocorrelation bias introduced by random sample division. After spatially independent training, the AUC values of CNN, XGBoost, and RF were 0.882, 0.863, and 0.847, respectively. CNN consistently achieved the best performance across the spatial partitions, further confirming its robustness in different spatial subsets for landslide susceptibility assessment. Compared with machine learning models based on manually engineered features, CNN automatically extracted multi-scale spatial features through its convolutional architecture and effectively captured the spatial correlations among landslide conditioning factors, thereby better representing their complex nonlinear relationships. Consequently, CNN demonstrated superior generalization ability and adaptability in landslide susceptibility assessment.

Table 5 counts the proportions of areas corresponding to different susceptibility classes for each model. The frequency ratio (FR) is calculated as the ratio between the percentage of landslide area within a given susceptibility class and the percentage of the total area occupied by that class in the study area, which further evaluates the accuracy of LSM. In general, the larger the FR value for high susceptibility areas and the smaller the FR value for low susceptibility areas, the more reliable the susceptibility prediction results. The results showed that the CNN model achieved high prediction accuracy in the probabilistic prediction of landslide susceptibility assessment. Figure 11 visualizes the FR results of the three models, the results showed that the frequency ratio of landslides increases with the increase in landslide susceptibility class, with very high susceptibility areas exhibiting much higher frequency ratios than very low susceptibility areas, which further proved that the CNN model demonstrated better discriminative ability and reliability in landslide susceptibility prediction, making it more applicable to the accurate assessment of landslide susceptibility.

Table 5. Statistical analysis of landslide susceptibility for each model.

Method	Susceptibility	Area (km^2)	Area Ratio (%)	Landslide Area (km^2)	Landslide Area Ratio (%)	FR (%)
CNN	Very Low	157.91	50.42	0	0	0
	Low	59.97	19.15	0.01	0.14	0.01
	Moderate	46.24	14.76	0.11	1.74	0.12
	High	30.98	9.89	0.92	14.30	1.45
	Very High	18.09	5.78	5.42	83.82	14.51

Table 5. *Cont.*

Method	Susceptibility	Area (km^2)	Area Ratio (%)	Landslide Area (km^2)	Landslide Area Ratio (%)	FR (%)
RF	Very Low	167.64	53.53	1.87	28.99	0.54
	Low	59.21	18.91	0.64	9.95	0.53
	Moderate	31.35	10.01	0.69	10.61	1.06
	High	25.05	7.99	0.79	12.25	1.53
	Very High	29.93	9.56	2.47	38.20	4.0
XGBoost	Very Low	146.39	46.74	0.88	13.62	0.29
	Low	59.65	19.05	0.99	15.40	0.81
	Moderate	37.39	11.94	0.67	10.36	0.87
	High	33.93	10.83	0.97	15.06	1.39
	Very High	35.82	11.44	2.95	45.57	3.98

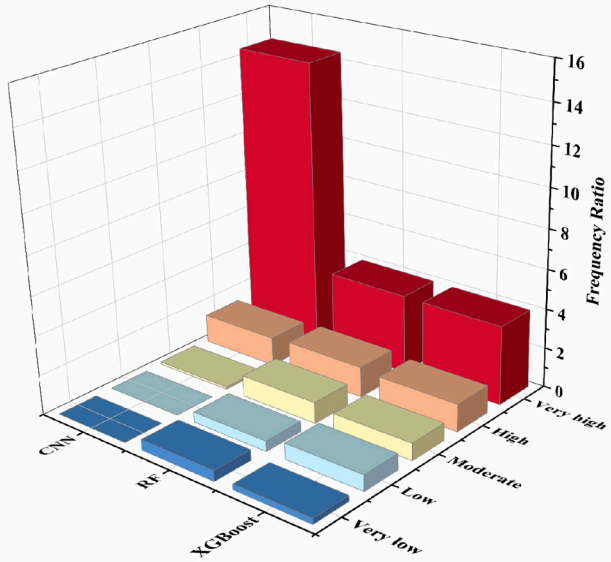


Figure 11. Comparison of model frequency ratio accuracy.

5. Discussion

5.1. Analysis of LSM Results

Figure 12 shows the altitude background of the study area, together with local enlarged views of landslide susceptibility maps generated by different models in the same region. From the altitude distribution and the locations of landslide sites in Figure 12a, the landslides in the study area are not simply concentrated in the high-elevation region but are mainly distributed in the mid-to-high-altitude zone where the terrain is more undulating, and the slopes are strongly cut. The local zoom results in Figure 12b–d show that the very high and high susceptibility zones identified by the CNN model in the local area are more consistent with the actual occurrence of landslides, which can better reflect the spatial clustering characteristics of landslides under complex terrain conditions. In contrast, the RF and XGBoost models predicted very high and high susceptibility zones in a relatively discrete range, with no landslide records in some areas, which are weaker than the CNN model in portraying the complex terrain background.

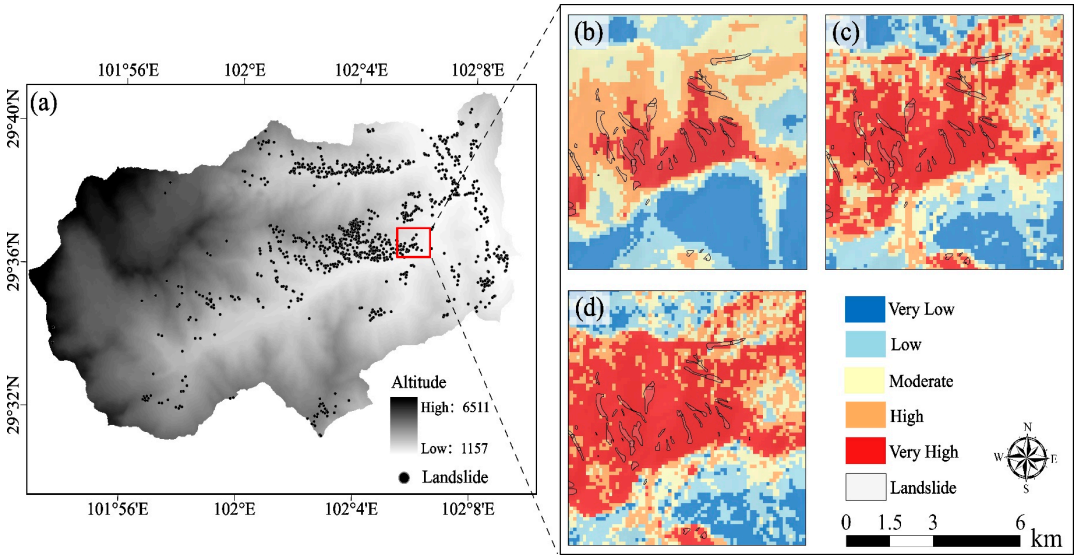


Figure 12. Local zoomed-in view of Figure 9: (**a**) altitude and landslide information; (**b**) CNN; (**c**) RF; (**d**) XGBoost.

5.2. SHAP-Based Explanability of CNN Model Predictions

To reveal the internal mechanism of the CNN model for landslide susceptibility discrimination, the SHAP method is employed to interpret the model decision process. Figure 13 presents the SHAP-based feature importance ranking and the distribution of their impacts on the model output. The contribution analysis of LCFs indicates that aspect, NDVI, distance to rivers, and altitude exhibit higher importance, and these factors serve as the primary controlling variables influencing the model predictions. The swarm distribution characteristics further exhibit the nonlinear relationship between the influencing factor values and the model outputs. Lower NDVI values correspond to more positive SHAP values, indicating that areas with sparse vegetation cover are more prone to landslide occurrence. In contrast, distance to rivers shows a positive relationship with the predicted results, and the areas closer to rivers are less susceptible to landslides. This pattern can be attributed to the presence of relatively gentle river terraces in the study area, which exhibit higher stability than the steeper slopes located farther from river channels. In contrast, the influence of altitude exhibits a distinct nonlinear pattern across altitude intervals. Rather than following a monotonic trend, SHAP values increase markedly within the mid-to-high altitude range, which corresponds to the zone where landslides are more densely distributed. This observation is consistent with the higher landslide density in mid-to-high altitude areas shown in Figure 12.

However, relying solely on variable contribution cannot fully demonstrate the model's geomorphological validity [30,55]. Therefore, we further analyzed the SHAP dependency relationships of the key factors in the context of the actual terrain of Moxi Town (Figure 14), highlighting their geomorphological significance. The SHAP values for NDVI indicate that low-to-medium vegetation coverage (0.4–0.7) positively contributes to landslide susceptibility, whereas high vegetation coverage (0.9–1.0) exerts a negative contribution. This pattern is consistent with field observations: the 2022 Luding earthquake damaged slope vegetation, and subsequent reconstruction and engineering activities further aggravated vegetation degradation, making areas with frequent human activity hotspots for landslides; in contrast, high-altitude primary forests with well-developed root systems stabilize slopes, reducing landslide probability. Areas within 5000 m of rivers, such as river valley terraces and gentle alluvial plains, exhibit inhibitory effects on landslides, whereas regions above approximately 6000 m show positive contributions, reflecting the greater stability

of river-adjacent gentle terraces compared with distant steep slopes. This spatial pattern demonstrates the slope stability differences controlled by river valley geomorphology. Regarding elevation, slopes at 2400–3500 m exhibit inhibitory effects, while the 3500–6200 m middle-to-high altitude range represents the core landslide-prone zone. Although areas above 6200 m still display high SHAP peaks, the points are highly dispersed, indicating that only a few steep cliff faces may trigger earthquake-induced high-altitude rockfalls, whereas the main snow and glacier areas lack conditions for landslide occurrence, which aligns well with the actual geomorphological characteristics of the region.

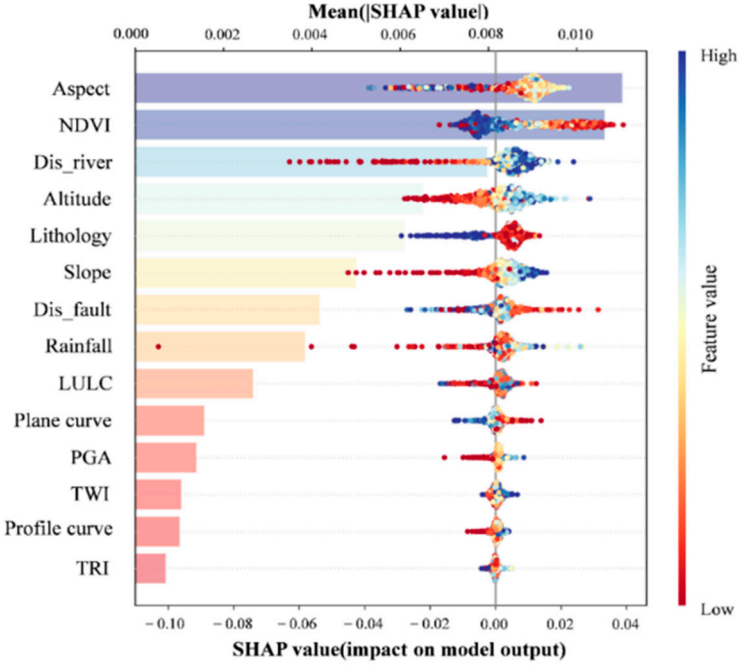


Figure 13. SHAP-based feature importance and swarm distribution for the CNN model.

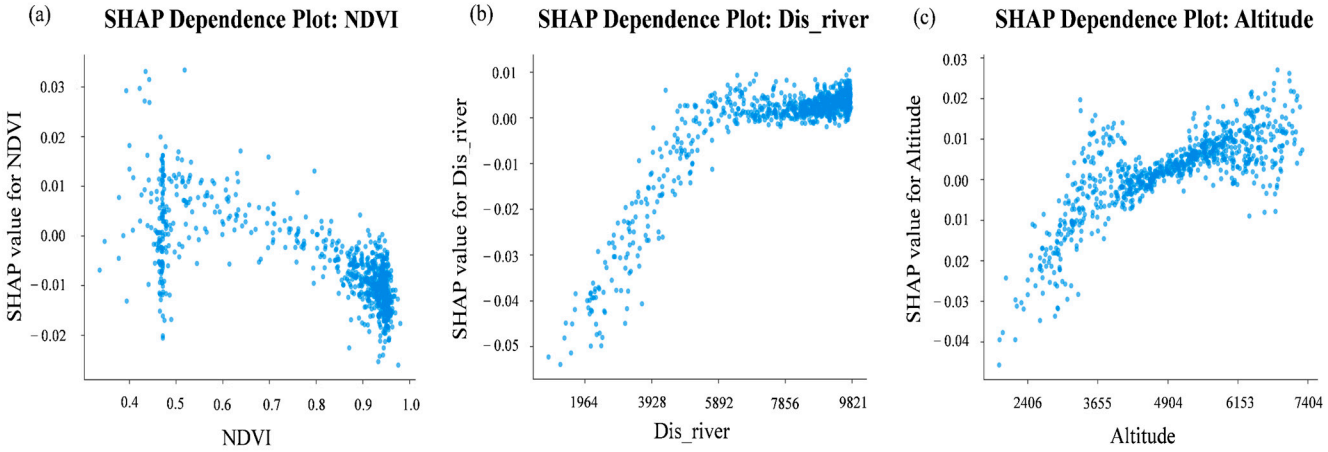


Figure 14. SHAP-based dependency plots of key controlling factors for the CNN model: (**a**) NDVI; (**b**) Dis_river; (**c**) altitude.

The contribution patterns of these factors reflect the combined effects of post-earthquake geological disturbances and human activities in Moxi Town. Their joint influence shapes the spatial landslide susceptibility patterns, which align closely with the actual geomorphological conditions, demonstrating that the model effectively captures the mechanisms controlling landslide formation.

5.3. Limitations and Future Work

This study presents preliminary results in landslide susceptibility prediction, but several limitations remain. First, the landslide dataset lacks type annotations (e.g., rotational slides, translational slides, and debris flows), which prevents the model from distinguishing the effects of different landslide types. Future work will incorporate high-resolution imagery and field surveys to classify landslide types, thereby enhancing the interpretability of the model.

Second, the model depends strongly on the geomorphological characteristics of the study area, and its transferability to other regions has not yet been evaluated. Moreover, temporal dynamics of landslide occurrence are not considered. Future research will integrate multi-temporal remote sensing or DEM datasets and explore transfer learning approaches to improve the applicability and generalization of the model across different regions and time scales.

6. Conclusions

In this study, a deep learning-based LSA framework was constructed for Moxi Town, realizing an integrated workflow from automatic landslide identification to susceptibility assessment. By comparing Mask R-CNN models with different combinations of backbone networks and optimizers, ResNet50 + AdamW was identified as the optimal configuration. Under an IoU threshold of $\geq$0.5, the target detection and instance segmentation accuracies reached 83.8% and 81.8%, respectively. Based on this optimal model, a landslide inventory containing 923 landslide samples was subsequently constructed. The CNN-based landslide susceptibility model was constructed by learning the spatial relationships between the landslide inventory and 14 influencing factors. A performance comparison with the RF and XGBoost machine learning models showed that the CNN model achieved the best overall performance, with an AUC value of 0.97. In addition, the susceptibility maps generated by the CNN model exhibited better spatial continuity, effectively suppressing the salt-and-pepper noise commonly observed in machine learning-based results. Frequency ratio analysis showed that the FR value of the CNN model increased progressively from 0 in the very low susceptibility zone to 14.51 in the very high susceptibility zone, further confirming the statistical consistency between the predicted susceptibility pattern and the observed landslide distribution. Finally, the interpretability analysis using the SHAP method clarifies the dominant role mechanism of key factors such as NDVI and river in the landslide occurrence in Moxi Town.

Overall, the framework proposed in this study demonstrated precise landslide identification capability and high-resolution susceptibility evaluation, integrating model interpretability with practical application value, and providing a novel approach for disaster prevention and mitigation in alpine valley areas.

Author Contributions: Conceptualization, W.Z. and X.L.; methodology, Y.Y. (Yitong Yao) and Y.D.; software, Y.Y. (Yitong Yao) and Y.D.; validation, Y.Y. (Yitong Yao) and X.L.; formal analysis, J.C. and H.F.; investigation, H.X. and R.H.; resources, Y.Y. (Yuhao Yang) and T.F.; data curation, Y.Y. (Yitong Yao), X.L. and J.C.; writing—original draft preparation, Y.Y. (Yitong Yao); writing—review and editing, Y.D., W.Z. and J.C.; visualization, Y.Y. (Yitong Yao); supervision, W.Z. and Y.D.; project administration, W.Z., J.C. and X.L.; funding acquisition, Y.D. and W.Z. All authors have read and agreed to the published version of the manuscript.

Funding: This research was funded by the National Natural Science Foundation of China (U22A20565, 42401101), the Sichuan Science and Technology Program (2026NSFSC1135), the Science and Technology Open Foundation of Sichuan Society of Surveying and Mapping Geoinformation (CCX202501), the Central Government Guided Local Science and Technology Development Fund Projects (202502ZYDF034), the Supply–Demand Matching for Employment and Talent Cultivation Project of

the Ministry of Education of China (2025050790134), and Technology Innovation Center for Emergency Surveying and Mapping, MNR (YJCX-2026-YB-03-01).

Data Availability Statement: The data used in this paper are available from the first and corresponding authors upon reasonable request. As these data are being prepared for a related paper, these data are not available to the public at this time.

Acknowledgments: The authors gratefully acknowledge the providers of open-access remote sensing and geospatial data used in this study, and thank Xu et al. [31] for releasing the CAS Landslide Dataset, which was used as the landslide inventory. The authors also thank Chang Guang Satellite Technology Co., Ltd., for providing Jilin-1 satellite imagery.

Conflicts of Interest: Author Yixiang Du was employed by the company Sichuan Zhentong Inspection Co., Ltd. The remaining authors declare that the research was conducted in the absence of any commercial or financial relationships that could be construed as a potential conflict of interest.

Abbreviations

The following abbreviations are used in this manuscript:

LSM	landslide susceptibility mapping
LSA	landslide susceptibility assessment
CNN	convolutional neural network
RF	random forest
XGBoost	extreme gradient boosting
SHAP	SHapley Additive exPlanations
LCFs	landslide conditioning factors

References

1. Zhou, C.; Gan, L.; Cao, Y.; Wang, Y.; Segoni, S.; Shi, X.; Motagh, M.; Singh, R.P. Landslide susceptibility assessment of the Wanzhou district: Merging landslide susceptibility modelling (LSM) with InSAR-derived ground deformation map. *Int. J. Appl. Earth Obs. Geoinf.* **2025**, *136*, 104365. [CrossRef]
2. Zhou, X.; Wen, H.; Zhang, Y.; Xu, J.; Zhang, W. Landslide Susceptibility Mapping Using Hybrid Random Forest with GeoDetector and RFE for Factor Optimization. *Geosci. Front.* **2021**, *12*, 101211. [CrossRef]
3. Bozzolan, E.; Holcombe, E.A.; Pianosi, F.; Marchesini, I.; Alvioli, M.; Wagener, T. A Mechanistic Approach to Include Climate Change and Unplanned Urban Sprawl in Landslide Susceptibility Maps. *Sci. Total Environ.* **2023**, *858*, 159412. [CrossRef]
4. Huang, F.; Liu, K.; Jiang, S.; Catani, F.; Liu, W.; Fan, X.; Huang, J. Optimization method of conditioning factors selection and combination for landslide susceptibility prediction. *J. Rock Mech. Geotech. Eng.* **2025**, *17*, 722–746. [CrossRef]
5. Jaafari, A.; Panahi, M.; Pham, B.T.; Shahabi, H.; Bui, D.T.; Rezaie, F.; Lee, S. Meta Optimization of an Adaptive Neuro-Fuzzy Inference System with Grey Wolf Optimizer and Biogeography-Based Optimization Algorithms for Spatial Prediction of Landslide Susceptibility. *CATENA* **2019**, *175*, 430–445. [CrossRef]
6. Zhang, T.; Li, Y.; Wang, T.; Wang, H.; Chen, T.; Sun, Z.; Luo, D.; Li, C.; Han, L. Evaluation of Different Machine Learning Models and Novel Deep Learning-Based Algorithm for Landslide Susceptibility Mapping. *Geosci. Lett.* **2022**, *9*, 26. [CrossRef]
7. Wang, Y.; Ling, Y.; Chan, T.O.; Awange, J. High-Resolution Earthquake-Induced Landslide Hazard Assessment in Southwest China through Frequency Ratio Analysis and LightGBM. *Int. J. Appl. Earth Obs. Geoinf.* **2024**, *131*, 103947. [CrossRef]
8. Liu, R.; Yang, X.; Xu, C.; Wei, L.; Zeng, X. Comparative Study of Convolutional Neural Network and Conventional Machine Learning Methods for Landslide Susceptibility Mapping. *Remote Sens.* **2022**, *14*, 321. [CrossRef]
9. Achour, Y.; Boumezbeur, A.; Hadji, R.; Chouabbi, A.; Cavaleiro, V.; Bendaoud, E.A. Landslide susceptibility mapping using analytic hierarchy process and information value methods along a highway road section in Constantine, Algeria. *Arab. J. Geosci.* **2017**, *10*, 194. [CrossRef]
10. Huang, F.; Yao, C.; Liu, W.; Li, Y.; Liu, X. Landslide susceptibility assessment in the Nantian area of China: A comparison of frequency ratio model and support vector machine. *Geomat. Nat. Hazards Risk* **2018**, *9*, 919–938. [CrossRef]
11. Roy, J.; Saha, S.; Arabameri, A.; Blaschke, T.; Bui, D.T. A Novel Ensemble Approach for Landslide Susceptibility Mapping (LSM) in Darjeeling and Kalimpong Districts, West Bengal, India. *Remote Sens.* **2019**, *11*, 2866. [CrossRef]
12. Arabameri, A.; Saha, S.; Roy, J.; Chen, W.; Blaschke, T.; Bui, D.T. Landslide Susceptibility Evaluation and Management Using Different Machine Learning Methods in the Gallicash River Watershed, Iran. *Remote Sens.* **2020**, *12*, 475. [CrossRef]

13. Chen, W.; Xie, X.; Peng, J.; Shahabi, H.; Hong, H.; Bui, D.T.; Duan, Z.; Li, S.; Zhu, A.-X. GIS-Based Landslide Susceptibility Evaluation Using a Novel Hybrid Integration Approach of Bivariate Statistical Based Random Forest Method. *CATENA* **2018**, *164*, 135–149. [CrossRef]
14. Fang, Z.; Wang, Y.; Duan, G.; Peng, L. Landslide Susceptibility Mapping Using Rotation Forest Ensemble Technique with Different Decision Trees in the Three Gorges Reservoir Area, China. *Remote Sens.* **2021**, *13*, 238. [CrossRef]
15. Huang, Y.; Zhao, L. Review on Landslide Susceptibility Mapping Using Support Vector Machines. *CATENA* **2018**, *165*, 520–529. [CrossRef]
16. Wang, Y.; Duan, H.; Hong, H. A Comparative Study of Composite Kernels for Landslide Susceptibility Mapping: A Case Study in Yongxin County, China. *CATENA* **2019**, *183*, 104217. [CrossRef]
17. Amatya, P.; Kirschbaum, D.; Stanley, T. Use of Very High-Resolution Optical Data for Landslide Mapping and Susceptibility Analysis along the Karnali Highway, Nepal. *Remote Sens.* **2019**, *11*, 2284. [CrossRef]
18. Chen, W.; Zhao, X.; Shahabi, H.; Shirzadi, A.; Khosravi, K.; Chai, H.; Li, R. Spatial prediction of landslide susceptibility by combining evidential belief function, logistic regression and logistic model tree. *Geocarto Int.* **2019**, *34*, 1177–1201. [CrossRef]
19. Chen, Y.; Ming, D.; Ling, X.; Lv, X.; Zhou, C. Landslide Susceptibility Mapping Using Feature Fusion-Based CPCNN-ML in Lantau Island, Hong Kong. *IEEE J. Sel. Top. Appl. Earth Obs. Remote Sens.* **2021**, *14*, 3625–3639. [CrossRef]
20. Nikoobakht, S.; Azarafza, M.; Akgün, H.; Derakhshani, R. Landslide Susceptibility Assessment by Using Convolutional Neural Network. *Appl. Sci.* **2022**, *12*, 5992. [CrossRef]
21. Melchiorre, C.; Matteucci, M.; Remondo, J. Artificial Neural Networks and Robustness Analysis in Landslide Susceptibility Zonation. In Proceedings of the IEEE International Joint Conference on Neural Networks, Vancouver, BC, Canada, 16–21 July 2006; pp. 4375–4381. [CrossRef]
22. Ge, Y.; Liu, G.; Tang, H. Comparative analysis of five convolutional neural networks for landslide susceptibility assessment. *Bull. Eng. Geol. Environ.* **2023**, *82*, 377. [CrossRef]
23. Wei, X.; Zhang, L.; Luo, J. A hybrid framework integrating physical model and convolutional neural network for regional landslide susceptibility mapping. *Nat. Hazards* **2021**, *109*, 471–497. [CrossRef]
24. Yang, X.; Liu, R.; Yang, M.; Chen, J.; Liu, T.; Yang, Y.; Chen, W.; Wang, Y. Incorporating Landslide Spatial Information and Correlated Features among Conditioning Factors for Landslide Susceptibility Mapping. *Remote Sens.* **2021**, *13*, 2166. [CrossRef]
25. Yang, Y.; Wang, R.; Guo, N. Future and present susceptibility to thermokarst hazards in the Northern Hemisphere using an interpretable CNN method. *J. Hydrol.* **2025**, *661*, 133787. [CrossRef]
26. Sameen, M.I.; Pradhan, B.; Lee, S. Application of Convolutional Neural Networks Featuring Bayesian Optimization for Landslide Susceptibility Assessment. *CATENA* **2020**, *186*, 104249. [CrossRef]
27. Dikshit, A.; Pradhan, B.; Alamri, A.M. Pathways and Challenges of the Application of Artificial Intelligence to Geohazards Modelling. *Gondwana Res.* **2021**, *100*, 290–301. [CrossRef]
28. Ozturk, U.; Pittore, M.; Behling, R. How robust are landslide susceptibility estimates? *Landslides* **2021**, *18*, 681–695. [CrossRef]
29. He, K.; Gkioxari, G.; Dollár, P.; Girshick, R. Mask R-CNN. In Proceedings of the IEEE International Conference on Computer Vision (ICCV), Venice, Italy, 22–29 October 2017; pp. 2961–2969.
30. Fu, R.; He, J.; Liu, G.; Li, W.; Mao, J.; He, M.; Lin, Y. Fast Seismic Landslide Detection Based on Improved Mask R-CNN. *Remote Sens.* **2022**, *14*, 3928. [CrossRef]
31. Xu, Y.; Ouyang, C.; Xu, Q.; Wang, D.; Zhao, B.; Luo, Y. CAS Landslide Dataset: A Large-Scale and Multisensor Dataset for Deep Learning-Based Landslide Detection. *Sci. Data* **2024**, *11*, 12. [CrossRef]
32. Pradhan, B.; Dikshit, A.; Lee, S.; Kim, H. An Explainable AI (XAI) Model for Landslide Susceptibility Modeling. *Appl. Soft Comput.* **2023**, *142*, 110324. [CrossRef]
33. Martinello, C.; Delchiaro, M.; Iacobucci, G.; Cappadonia, C.; Rotigliano, E.; Piacentini, D. Exploring the geomorphological adequacy of the landslide susceptibility maps: A test for different types of landslides in the Bidente river basin (northern Italy). *CATENA* **2024**, *238*, 107835. [CrossRef]
34. Cui, F.; Ning, M.; Shen, J.; Shu, X. Automatic Recognition and Tracking of Highway Layer-Interface Using Faster R-CNN. *J. Appl. Geophys.* **2022**, *196*, 104477. [CrossRef]
35. Long, J.; Shelhamer, E.; Darrell, T. Fully Convolutional Networks for Semantic Segmentation. In Proceedings of the IEEE Conference on Computer Vision and Pattern Recognition (CVPR), Boston, MA, USA, 7–12 June 2015; pp. 3431–3440.
36. Ren, S.; He, K.; Girshick, R.; Sun, J. Faster R-CNN: Towards Real-Time Object Detection with Region Proposal Networks. *IEEE Trans. Pattern Anal. Mach. Intell.* **2017**, *39*, 1137–1149. [CrossRef]
37. Pazhani, A.A.J.; Vasanthanayaki, C. Object detection in satellite images by faster R-CNN incorporated with enhanced ROI pooling (FrRNet-ERoI) framework. *Earth Sci. Inform.* **2022**, *15*, 553–561. [CrossRef]
38. Yan, C.; Chen, W.; Chen, P.C.Y.; Kendrick, A.S.; Wu, X. A new two-stage object detection network without RoI-Pooling. In Proceedings of the Chinese Control and Decision Conference (CCDC), Shenyang, China, 9–11 June 2018; pp. 1680–1685. [CrossRef]

39. Wang, J.; Chen, G.; Jaboyedoff, M.; Derron, M.-H.; Li, F.; Li, H.; Luo, X. Loess Landslides Detection via a Partially Supervised Learning and Improved Mask-RCNN with Multi-Source Remote Sensing Data. *CATENA* **2023**, *231*, 107371. [CrossRef]
40. Lin, T.-Y.; Maire, M.; Belongie, S.; Hays, J.; Perona, P.; Ramanan, D.; Dollár, P.; Zitnick, C.L. Microsoft COCO: Common Objects in Context. In *Computer Vision—ECCV 2014*; Springer: Cham, Switzerland, 2014; pp. 740–755.
41. Pradhan, B.; Seeni, M.I.; Nampak, H. Integration of LiDAR and QuickBird Data for Automatic Landslide Detection Using Object-Based Analysis and Random Forests. In *Laser Scanning Applications in Landslide Assessment*; Pradhan, B., Ed.; Springer: Cham, Switzerland, 2017; pp. 69–81. [CrossRef]
42. Hussain, M.A.; Chen, Z.; Zhou, Y.; Meena, S.R.; Ali, N.; Shah, S.U. Landslide susceptibility mapping using artificial intelligence models: A case study in the Himalayas. *Landslides* **2025**, *22*, 2089–2103. [CrossRef]
43. Hussain, M.A.; Chen, Z.; Zheng, Y.; Zhou, Y.; Daud, H. Deep Learning and Machine Learning Models for Landslide Susceptibility Mapping with Remote Sensing Data. *Remote Sens.* **2023**, *15*, 4703. [CrossRef]
44. Arabameri, A.; Saha, S.; Mukherjee, K.; Blaschke, T.; Chen, W.; Ngo, P.T.T.; Band, S.S. Modeling Spatial Flood Using Novel Ensemble Artificial Intelligence Approaches in Northern Iran. *Remote Sens.* **2020**, *12*, 3423. [CrossRef]
45. O'Brien, R.M. A Caution Regarding Rules of Thumb for Variance Inflation Factors. *Qual. Quant.* **2007**, *41*, 673–690. [CrossRef]
46. Appukuttan, A.; Deshpande, G.; Jadhav, A.; Reghunath, R. Geospatial Modeling of Landslide Susceptibility in Lateritic Terrain: Insights from Machine Learning Techniques—Random Forest and DBSCAN. *Discov. Appl. Sci.* **2025**, *7*, 1224. [CrossRef]
47. Wang, L.; Yang, K.; Wu, C.; Zhou, Y.; Liu, J.; Hu, H. Novel approach to quantitative risk assessment of reservoir landslides using a hybrid CNN-LSTM model. *Landslides* **2025**, *22*, 943–956. [CrossRef]
48. Ye, C.M.; Liu, X.; Xu, H. Classification of hyperspectral images based on a convolutional neural network and spectral sensitivity. *J. Zhejiang Univ. Sci. A* **2020**, *21*, 240–248. [CrossRef]
49. Kong, L.; Feng, W.; Yi, X.; Xue, Z.; Bai, L. Enhanced landslide susceptibility mapping in data-scarce regions via unsupervised few-shot learning. *Gondwana Res.* **2025**, *138*, 31–46. [CrossRef]
50. Schneider, M.J.; Gorr, W.L. ROC-Based Model Estimation for Forecasting Large Changes in Demand. *Int. J. Forecast.* **2015**, *31*, 253–262. [CrossRef]
51. An, B.; Zhang, Z.; Xiong, S.; Zhang, W.; Yi, Y.; Liu, Z.; Liu, C. Landslide Susceptibility Mapping Based on Ensemble Learning in the Jiuzhaigou Region, Sichuan, China. *Remote Sens.* **2024**, *16*, 4218. [CrossRef]
52. Youssef, A.M.; Pourghasemi, H.R.; Pourtaghi, Z.S. Landslide susceptibility mapping using random forest, boosted regression tree, classification and regression tree, and general linear models and comparison of their performance at Wadi Tayyah Basin, Asir Region, Saudi Arabia. *Landslides* **2016**, *13*, 839–856. [CrossRef]
53. Wang, Y.H.; Zhang, W.G.; Wang, L.Q.; Liu, S.L.; Zhang, K.Q.; Liu, P.F.; Sun, W.X.; Jiang, S.H. Cross-regional extrapolation of landslide susceptibility mapping via transfer learning. *Geosci. Front.* **2025**, *16*, 102212. [CrossRef]
54. Shapley, L.S. The Shapley Value. In *Handbook of Game Theory with Economic Applications*; Aumann, R.J., Hart, S., Eds.; Elsevier: Amsterdam, The Netherlands, 2002; Volume 3, pp. 2025–2054.
55. Delchiaro, M.; Rouhi, J.; Valiante, M.; Della Seta, M.; Esposito, C.; Martino, S. Bivariate landslide susceptibility analysis in the Lorestan Arc (Zagros Mountains, Iran). *Ital. J. Eng. Geol. Environ.* **2021**, *17*, 53–66. [CrossRef]

Disclaimer/Publisher's Note: The statements, opinions and data contained in all publications are solely those of the individual author(s) and contributor(s) and not of MDPI and/or the editor(s). MDPI and/or the editor(s) disclaim responsibility for any injury to people or property resulting from any ideas, methods, instructions or products referred to in the content.